Amphiphilic semiconducting polymer as multifunctional nanocarrier for fluorescence/photoacoustic imaging guided chemo-photothermal therapy

Jiang, Yuyan; Cui, Dong; Fang, Yuan; Zhen, Xu; Upputuri, Paul Kumar; Pramanik, Manojit; Ding, Dan; Pu, Kanyi

2017

Jiang, Y., Cui, D., Fang, Y., Zhen, X., Upputuri, P. K., Pramanik, M., et al. (2017). Amphiphilic semiconducting polymer as multifunctional nanocarrier for fluorescence/photoacoustic imaging guided chemo-photothermal therapy. Biomaterials, in press.

https://hdl.handle.net/10356/85147

https://doi.org/10.1016/j.biomaterials.2017.08.037

Amphiphilic Semiconducting Polymer as Multifunctional Nanocarrier for Fluorescence/Photoacoustic Imaging Guided Chemo-Photothermal Therapy

Yuyan Jiang [a], Dong Cui [a], Yuan Fang [b], Xu Zhen [a], Paul Kumar Upputuri [a], Manojit Pramanik [a], Dan Ding [b], and Kanyi Pu [a, *]

[a]*School of Chemical and Biomedical Engineering, Nanyang Technological University, 70 Nanyang Drive, 637459, Singapore*
[b]*State of Key Laboratory of Medicinal Chemical Biology, Key Laboratory of Bioactive Materials, Ministry of Education, College of Life Sciences, Nankai University, Tianjin 300071, China*
**Corresponding author: E-mail address: kypu@ntu.edu.sg (K. Pu)*

Keywords: Semiconducting polymer nanoparticles, photoacoustic imaging, photothermal therapy, near-infrared fluorescence imaging, drug delivery

Abstract: Chemo-photothermal nanotheranostics has the advantage of synergistic therapeutic effect, providing opportunities for optimized cancer therapy. However, current chemo-photothermal nanotheranostic systems generally comprise more than three components, encountering the potential issues of unstable nanostructures and unexpected conflicts in optical and biophysical properties among different components. We herein synthesize an amphiphilic semiconducting polymer (PEG-PCB) and utilize it as a multifunctional nanocarrier to simplify chemo-photothermal nanotheranostics. PEG-PCB has a semiconducting backbone that not only serves as the diagnostic component for near-infrared (NIR) fluorescence and photoacoustic (PA) imaging, but also acts as the therapeutic agent for photothermal therapy. In addition, the hydrophobic backbone of PEG-PCB provides strong hydrophobic and π-π interactions with the aromatic anticancer drug such as doxorubicin for drug encapsulation and delivery. Such a trifunctionality of PEG-PCB eventually results in a greatly simplified nanotheranostic system with only two components but multimodal imaging and therapeutic capacities, permitting effective NIR fluorescence/PA imaging guided chemo-photothermal therapy of cancer in living

mice. Our study thus provides a molecular engineering approach to integrate essential properties into one polymer for multimodal nanotheranostics.

1. Introduction

Development of nanotechnology in the past few decades has stimulated the emergence of nanotheranostics for simultaneous diagnosis and therapeutics of diseases.[1] Nanotheranostics has the ability to monitor disease status before and during treatment, providing optimized therapeutic window and personalized treatment strategy.[2-4] Recently, chemo-phototherapy has been regarded as a promising treatment for solid tumors.[5-7] In particular, chemo-photothermal nanotheranostics integrating anticancer drug with thermal ablation not only overcomes the multidrug resistance of conventional chemotherapy, but also brings in synergistic therapeutic effect to improve therapeutic outcome.[8-10] Such combined nanotheranostics thus has the potential advantages of reduced risk of cancer recurrence and minimized side effects relative to monotherapy.[11]

Current chemo-photothermal nanotheranostic systems often use fluorescence for diagnosis mainly due to its low cost and high sensitivity for whole-body imaging.[12, 13] However, fluorescence imaging often encounters the issue of shallow penetration depth as a result of tissue autofluorescence and light scattering.[14, 15] Thus, photoacoustic (PA) imaging that breaks the optical diffusion limit has recently been integrated into chemo-photothermal nanotheranostics, which has the advantage of increased imaging depth theoretically up to 7 cm.[16-21] Till now, numerous theranostic nanoagents have been exploited for chemo-photothermal therapy, such as 2D nanomaterials,[22-25] gold nanostructures,[26, 27] carbon-metal composites,[28] small-molecule dye loaded nanoparticles,[29] and so on.[30] However, because most chemo-photothermal nanotheranostic systems comprise more than three components (imaging agents, drug, photothermal agents and encapsulating polymers et al.),

clinical translation of these nanotheranostics faces many challenges, which include complex and unstable nanostructure as well as unexpected conflicts in optical and biophysical properties among different components. As a result, rational design of nanotheranostics with minimal components and simple nanostructure is highly desired.

Semiconducting polymer nanoparticles (SPNs) have been recently transformed to organic theranostic nanoagents owning to their higher absorption and photothermal conversion efficiencies in near-infrared (NIR) region as compared with other inorganic nanoparticles such as carbon nanotubes and gold nanorods.[31-37] Because their optical and photothermal properties come from long π-electron delocalized backbones, SPNs generally possess better photostability than small-molecule dyes.[38] Recently, we have applied SPNs for fluorescence and PA imaging applications as well as photothermal therapy and control of neural activity.[39-47] Despite their promise in nanotheranostics, SPN-based chemo-photothermal systems are rarely developed,[48-50] which are complicated and composed of more than three components.

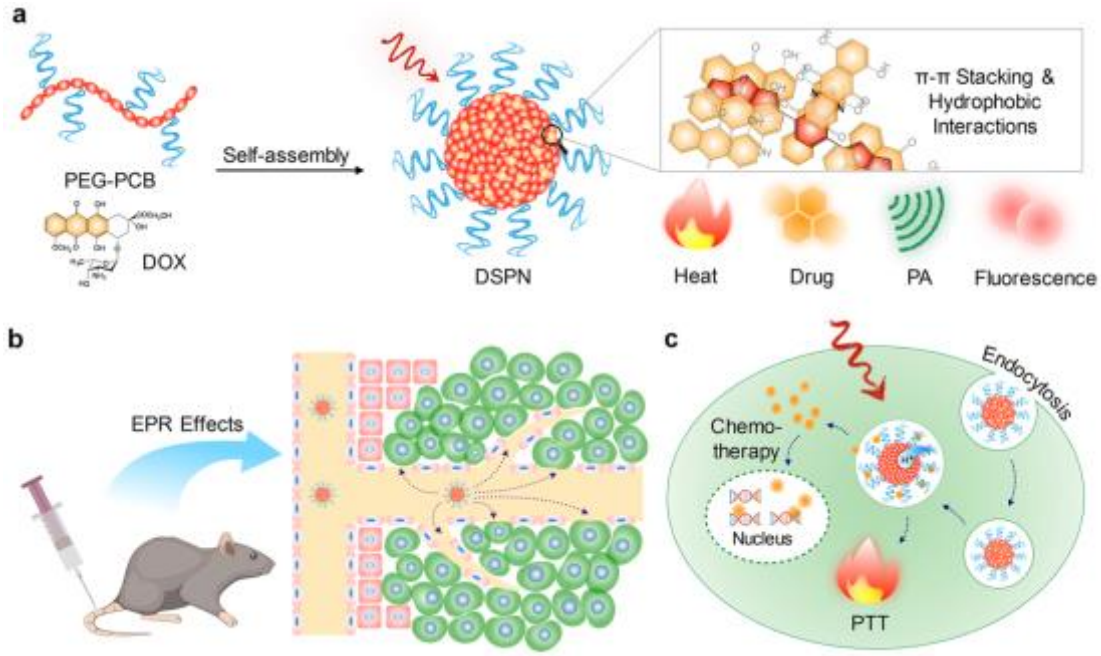

Scheme 1. (a) Schematic illustration of preparation of DSPN. (b) and (c) Synergistic effect of chemotherapy and PTT of cancer by DSPN.

In this study, we report a simple dual-component nanotheranostic system based on SPNs for NIR fluorescence/PA imaging guided chemo-photothermal therapy (Scheme 1a). Such a nanotheranostic design takes advantage of an amphiphilic poly(ethylene glycol) (PEG) grafted poly(cyclopentadithiophene-*alt*-benzothiadiazole) (PEG-PCB), which is a highly integrated multifunctional component that self-assembles into homogenous nanoparticles in aqueous solution. As a result of π-conjugated backbone, PEG-PCB not only serves as the diagnostic component for NIR fluorescence and PA imaging, but also acts as the photothermal agent by efficiently converting photon energy into heat. In addition, the hydrophobic π-conjugated backbone of PEG-PCB provides strong hydrophobic and π-π interactions with the aromatic anticancer drug such as doxorubicin (DOX) for drug encapsulation and delivery. Such a unique trifunctional feature of PEG-PCB leads to the greatly simplified nanotheranostic system with only dual components but multimodal imaging and therapeutic capacities. In the following, we first describe the synthesis and characterization of PEG-PCB and drug-loaded PEG-PCB (DSPN), followed by *in vitro* studies of the cellular internalization and chemo-photothermal therapeutic efficacy. At last, the proof-of-concept application of theranostic DSPN in fluorescence/PA imaging guided chemo-photothermal therapy of tumor in living mice is demonstrated.

2. Results and Discussion

The amphiphilic PEG-PCB was synthesized via a grafting-on approach (Fig. 1a). Monomers 1 and 2 were copolymerized via Suzuki polycondensation reaction to afford the polymer with bromide side groups (PCB-Br). The bromide groups were converted to azide, allowing for copper(I)-catalyzed azide-alkyne click reaction (CuAAC) to graft hydrophilic PEG chains onto highly hydrophobic polymer backbones. The resulted polymer (PEG-PCB) could be directly dissolved water and self-assemble into nanoparticles. Drug-loaded nanoparticles (DSPNs) were prepared via nanoprecipitation of deprotonated DOX and PEG-PCB under controlled pH

condition, followed by dialysis to remove excess free DOX. The solutions of nanoparticles kept translucent before and after drug loading (Fig. 1b), while the color of solutions changed from cyan to crimson owning to the incorporation of DOX. Dynamic light scattering (DLS) revealed the diameter increased from 40 nm for PEG-PCB to 100 nm for DSPN with the highest drug loading capacity (LC = 20.3%, W_{DOX}/W_{PCB} = 5, termed as $DSPN_5$) (Fig. 1c). Spherical morphology was observed for both PEG-PCB and $DSPN_5$ by transmission electron microscopy (TEM) (Fig. 1d). In addition, no precipitation or obvious change in diameter was observed for both PEG-PCB and $DSPN_5$ after storage in 1 × PBS (pH = 7.4) for two months, suggesting their excellent aqueous stability (Fig. S4, supporting information).

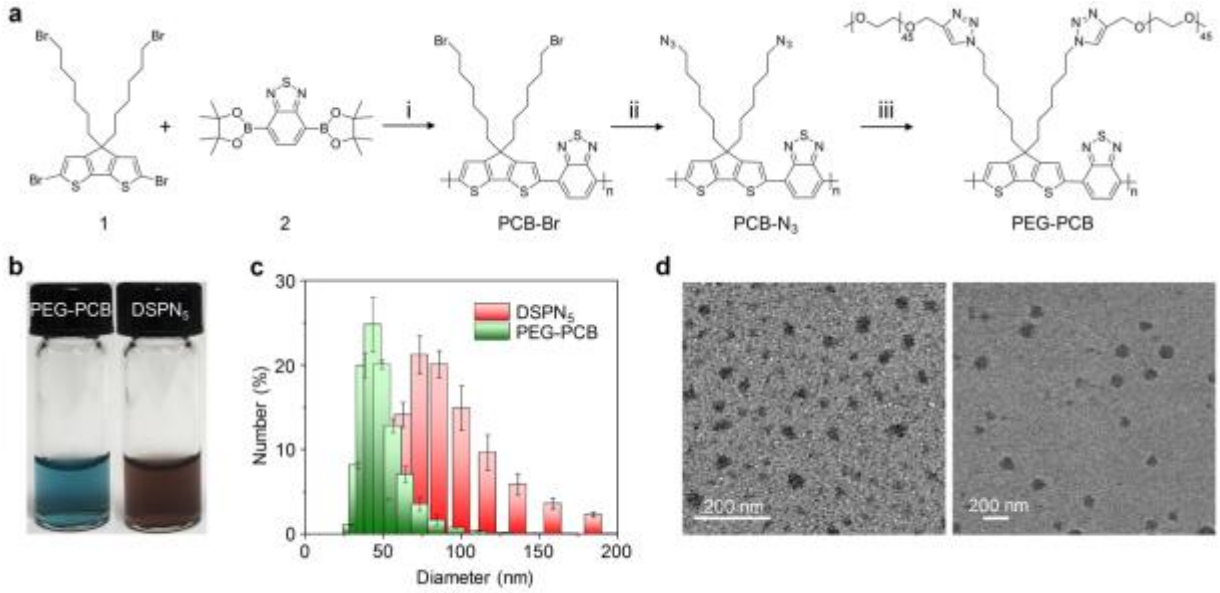

Fig. 1. Synthesis and characterization of PEG-PCB and $DSPN_5$. (a) Synthetic route of PEG-PCB. (i) $Pd(PPh_3)_4$, K_2CO_3, methyltrioctylammonium chloride, Toluene/H_2O; (ii) NaN_3; (iii) mPEG-alkyne, CuBr, PMDETA, THF. (b) Photographs of PEG-PCB and $DSPN_5$ solution. (PCB 10 μg/ml, DOX 50 μg/ml). (c) Size distribution of PEG-PCB and $DSPN_5$ by DLS. (d) TEM images of PEG-PCB (left) and $DSPN_5$ (right).

Optical properties of DSPN were studied and compared with PEG-PCB under physiological conditions. PEG-PCB had one absorption peak at 670 nm assigned to the absorbing PCB (Fig.

2a), while DSPN showed an additional absorption peak at 500 nm attributed to DOX. The absorbance of DSPN at 500 nm gradually increased with the doping ratio of DOX. Although the fluorescence spectra of SPN and DSPN had the emission maximum at 825 nm (Fig. 2b), the fluorescence was quenched after the loading of DOX. Compared with PEG-PCB, a 75% decrease of fluorescence intensity at 825 nm was observed for $DSPN_5$. Such fluorescence quenching should be attributed to the charge transfer between the π-conjugated polymer backbones and the anthraquinone part of DOX. Furthermore, both SPN and $DSPN_5$ emitted PA signals ranging from 680 to 900 nm with the peak signal at 680 nm (Fig. 2c), correlated well with their absorption spectra (Fig. 2a). As the fluorescence of $DSPN_5$ was quenched and that part of energy was converted into heat,[39] the PA amplitudes of $DSPN_5$ were slightly higher than those of PEG-PCB.

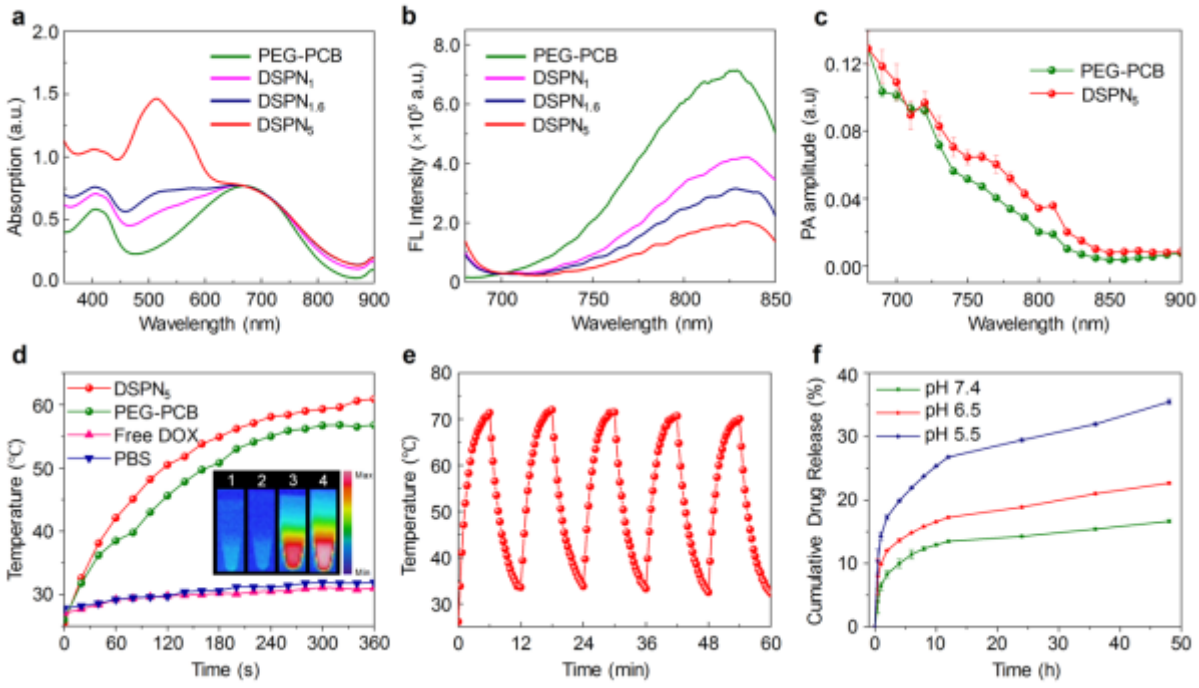

Fig. 2. *In vitro* optical, PA, photothermal, and drug release properties of PEG-PCB and DSPN in 1 × PBS. (a) UV-Vis-NIR absorption and (b) Fluorescence spectra of PEG-PCB and DSPN with different loading ratio (W_{DOX}/W_{PCB} = 1, 1.6, and 5 for $DSPN_1$, $DSPN_{1.6}$, and $DSPN_5$, respectively). Excitation wavelength, 670 nm. (c) PA spectra of PEG-PCB (PCB, 100 μg/ml)

and $DSPN_5$ (PCB, 100 μg/ml; DOX, 500 μg/ml). (d) Photothermal profiles, thermal images of PBS (1), free DOX (2) (DOX, 50 μg/ml), PEG-PCB (3) (PCB, 10 μg/ml), and $DSPN_5$ (4) (PCB, 10 μg/ml; DOX, 50 μg/ml) under irradiation of 808 nm laser (laser intensity, 1 W/cm^2). (e) Stability study of $DSPN_5$ under the photothermal heating and natural cooling cycles (laser intensity, 1 W/cm^2; PCB, 18 μg/ml; DOX, 90 μg/ml). (f) Cumulative drug release of $DSPN_5$ under different pH conditions at 37 ℃ (PCB, 0.2 mg/ml; DOX, 1 mg/ml). Error bars indicate standard deviations of 3 separate measurements.

Photothermal properties of PEG-PCB and $DSPN_5$ were subsequently investigated and compared. Under laser irradiation at 808 nm with the power intensity of 1 W/cm^2, the solution temperatures for both PEG-PCB and $DSPN_5$ gradually increased, which was not observed for PBS and free DOX solutions (Fig. 2d). After continuous laser irradiation for 6 min, the solution temperatures of both PEG-PCB and $DSPN_5$ reached a plateau. At this time point, the solution temperature of $DSPN_5$ (60.9 ºC) was about 4.1 ºC higher than that of PEG-PCB (56.8 ℃). Such slightly enhanced maximum photothermal temperature for $DSPN_5$ should be attributed to the additional heat generated by $DSPN_5$ as a result of quenched fluorescence. The reversible heating-cooling operation showed that the maximum solution temperatures of $DSPN_5$ retained almost unchanged throughout at least 5 heating-cooling cycles, indicating its good photostability (Fig. 2e). Besides, the photothermal conversion efficiency of $DSPN_5$ at 808 nm was calculated to be 30.8% according to the previously reported procedure.[40] In addition, drug release property of $DSPN_5$ was studied by dialysis of $DSPN_5$ in 1 × PBS buffer under different pH conditions (pH = 5.5, 6.5, and 7.4) at 37 ºC (Fig. 2f). After 48 h of dialysis, ~35.5% of DOX was released from $DSPN_5$ at pH 5.5, followed by 22.7% at pH 6.5 and 16.7% at pH 7.4. This pH-dependent drug release behavior should be attributed to the protonation of amine group of DOX under acidic conditions, which enhanced its hydrophilicity and facilitated its

escape from the hydrophobic core of $DSPN_5$. These results indicated that $DSPN_5$ had suitable photothermal and drug release properties for chemo-photothermal therapy.

To study the *in vitro* cellular uptake and drug release properties of nanoparticles, confocal laser scanning microscopy (CLSM) was conducted on murine breast cancer cells (4T1). After incubation with free DOX, PEG-PCB, or $DSPN_5$ for 12 h, cells were washed by PBS buffer and then stained with nuclear indicator 4',6-diamidino-2-phenylindole (DAPI, depicted in blue). NIR fluorescence (depicted in red) was observed for PEG-PCB or $DSPN_5$ treated cells (Fig. 3a), showing the cellular internalization of both nanoparticles. Moreover, the fluorescence of DOX was detected for $DSPN_5$ treated cells. Although the strongest signal from DOX was observed in cytoplasm, there was a signal overlap between the fluorescence of DOX and of DAPI (Fig. 3a). This data proved that DOX was released from $DSPN_5$ and diffused to nuclei, probably attributed to the protonation of amine group of DOX under acidic conditions in lysosomes (Scheme 1c), which enhanced the hydrophilicity of DOX and facilitated its escape from the hydrophobic core of $DSPN_5$.

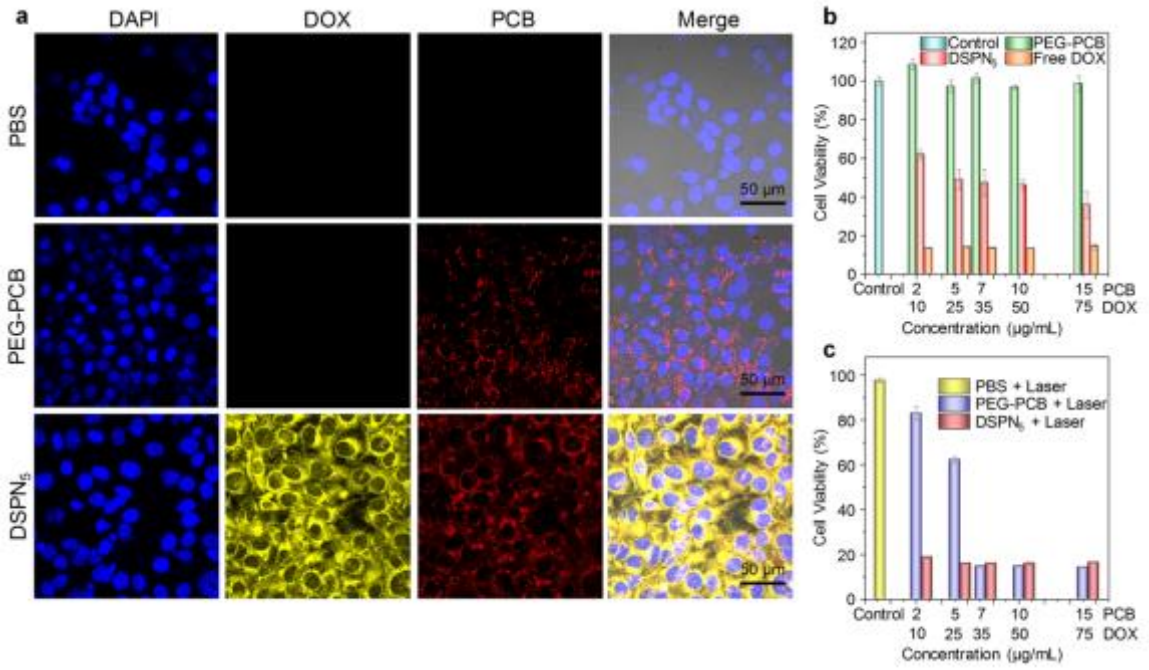

Fig. 3. *In vitro* characterization of combination therapy by $DSPN_5$. (a) Confocal fluorescence images of 4T1 cells after incubation with PBS, PEG-PCB (PCB, 10 μg/ml), and $DSPN_5$ (PCB,

10 μg/ml; DOX, 50 μg/ml) for 12 h. (b) Cell viabilities of 4T1 cells after incubation with PBS, free DOX, PEG-PCB, and $DSPN_5$ with different concentrations. (c) Cell viabilities of 4T1 cells after incubation with PBS, PEG-PCB, and $DSPN_5$ with different concentrations after laser irradiation for 6 min (laser intensity, 1 W/cm^2). Error bars indicate standard deviations of 3 separate measurements.

In vitro therapeutic efficacy of combination therapy vs monotherapy was evaluated and compared by cell viability tests. Without laser irradiation, PEG-PCB showed negligible toxicity to 4T1 cells while $DSPN_5$ had a significantly lower cell viability as compared with PEG-PCB at each concentration (Fig. 3b). This verified the increased cytotoxicity of $DSPN_5$ than PEG-PCB due to the presence of DOX, although the cytotoxicity was weaker than that of free DOX probably owning to the controlled release of DOX from $DSPN_5$ which somehow compromised the therapeutic efficacy (Fig. 3b). After irradiation of 808 nm laser for 6 min, cells incubated with PEG-PCB or $DSPN_5$ showed obvious decrease in viability at each concentration as compared to those without laser irradiation (Fig. 3c vs 3b), indicating the enhanced cytotoxicity owning to PTT. It was noted that $DSPN_5$ mediated PTT treatment caused the highest cytotoxicity among all the treatments. In particular, at the concentration of 2 μg/mL for PCB and 10 μg/mL for DOX, cell viability after $DSPN_5$ mediated PTT treatment was about 19%, which was much lower than that by $DSPN_5$ alone (62%) and SPN-mediated PTT (83%). Furthermore, PEG-PCB was only able to achieve similar cytotoxicity at a much higher concentration (7 μg/mL of PCB) (Fig. 3c), and $DSPN_5$ without PTT treatment was insufficient to cause such high cytotoxicity within experimental range (Fig. 3b). These results demonstrated the overall enhanced therapeutic efficacy of combination therapy relative to monotherapy, highlighting the synergistic antitumor effect of $DSPN_5$ for cancer therapy.

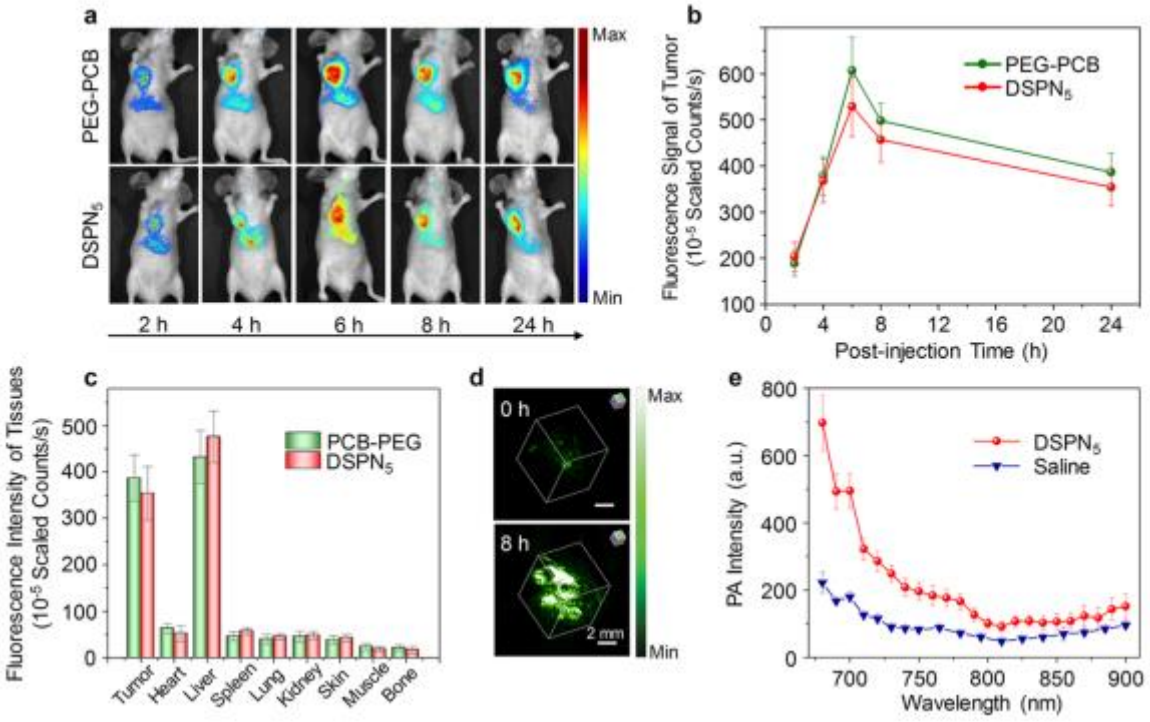

Fig. 4. *In vivo* dual-modal NIR fluorescence/PA tumor imaging. (a) Fluorescence images of living mice bearing xenograft 4T1 tumors at 0, 4, 6, 8 and 24 h after tail-vein injection of PEG-PCB (PCB 30 μg per mouse) or $DSPN_5$ (PCB, 30 μg; DOX, 150 μg per mouse) (n=3). (b) Fluorescence intensities extracted from tumor regions as a function of time after systemic administration of PEG-PCB or $DSPN_5$ (n=3). (c) *Ex vivo* quantification of average fluorescence intensity of major organs of mice after systemic administration of PEG-PCB or $DSPN_5$ for 24 h (n = 3). (d) Representative 3D images of tumor on a living mouse at 0 and 8 h after injection of $DSPN_5$ (PCB, 30 μg; DOX, 150 μg per mouse) (n=3). (e) *In vivo* real-time PA spectra extracted from tumor regions in living mice after systemic administration of $DSPN_5$ or saline for 24 h (n=3).

Dual-modal NIR fluorescence/PA imaging were conducted on living mice bearing 4T1 xenograft tumors to identify the optimum therapeutic window. After systemic administration of PEG-PCB or $DSPN_5$ *via* tail vein injection, both fluorescence and PA signals of living mice were continually monitored. As shown in Fig. 4a and b, the fluorescence intensities from the

tumor region for both PEG-PCB and $DSPN_5$ treated mice increased over time and reached the maximum at 6 h post-injection. At this time point, the fluorescence intensity of tumor region on $DSPN_5$ treated mice was 0.87-fold of that on PEG-PCB treated mice. The lower fluorescence intensity for $DSPN_5$ treated mice should be attributed to the quenching of fluorescence by DOX (Fig. 2b). Moreover, the decreased accumulation of $DSPN_5$ in tumors as indicated by the lower tumor-to-liver intensity ratio (TLR) of $DSPN_5$ vs PEG-PCB (1.0 vs 1.6) treated mice should be responsible (Fig. S6, supporting information), which could be ascribed to the relatively larger size of $DSPN_5$ than PEG-PCB. Similarly, the PA signal of tumor region reached the maximum at 8 h post-injection of DSPN (Fig. S7 and S8, supporting information). At this time point, the PA amplitude of tumor region in $DSPN_5$ treated mice was 3.8-fold higher than that of tumor background, which was consistent with the fluorescence imaging. As a result of the high optical contrast and spatial resolution of PA technique, 3D PA image after injection of $DSPN_5$ was able to clearly delineate the tumor region of living mouse (Fig. 4d). Real-time *in vivo* PA spectrum extracted from tumor regions of $DSPN_5$ treated mice (Fig. 4e) resembled that of $DSPN_5$ in aqueous solution (Fig. 2c), confirming that the PA signal resulted from the accumulation nanoparticles. *Ex vivo* data further revealed that liver had the strongest fluorescence for both PEG-PCB and $DSPN_5$ treated mice, followed by tumor, and other organs (Fig. 4c and Fig. S5, supporting information). No obvious change was measured between the biodistribution of PEG-PCB and $DSPN_5$ treated mice, probably due to their similar PEG surface. These in vivo and ex vivo imaging data proved that both PEG-PCB and $DSPN_5$ could passively target the tumors in living mice *via* enhanced permeability and retention (EPR) effect due to their idea sizes (within 100 nm) and PEGylated surface (Scheme 1b).

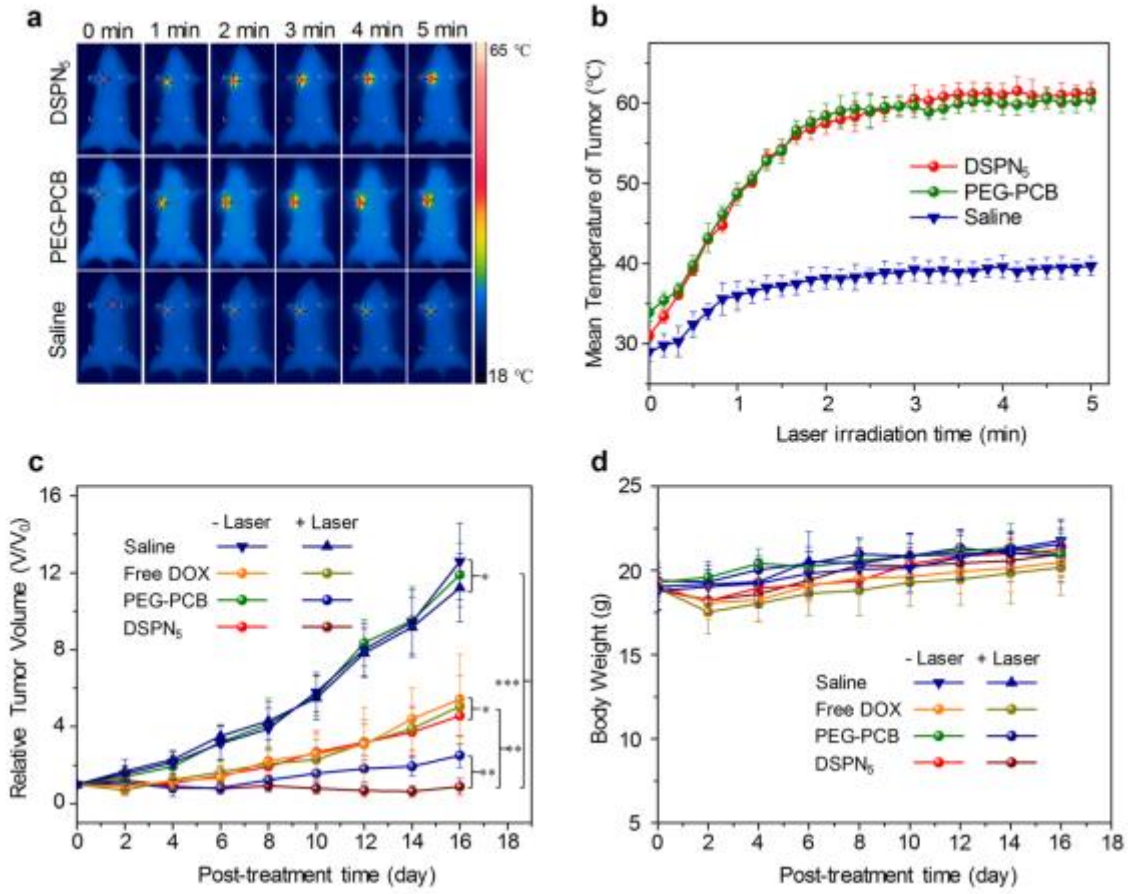

Fig. 5. *In vivo* combination therapy. (a) IR thermal images of 4T1-bearing mice under 808 nm laser irradiation (0.3 W/cm^2) at 6 h after systemic administration of saline, PEG-PCB (PCB 30 μg per mouse), or DSPN$_5$ (PCB, 30 μg; DOX, 150 μg per mouse) (n=3). (b) Mean tumor temperature as a function of laser irradiation time at 8 h post-injection of DSPN$_5$, PEG-PCB, or saline (n=3). (c) Tumor growth curves and (d) body weight data of different groups of mice after systemic administration of DSPN$_5$, PEG-PCB, or saline with and without laser irradiation (n = 3). (*$p > 0.05$, **$p < 0.05$, ***$p < 0.01$).

Therapeutic efficacy of PEG-PCB and DSPN$_5$ was tested and compared in 4T1 xenograft tumor mouse model. According to the *in vivo* imaging data, PTT treatment was applied at 6 h post-injection of PEG-PCB or DSPN$_5$ when the accumulation of nanoparticles in the tumor reached the maximum. After systemic administration of DSPN$_5$, PEG-PCB, or saline for 6 h, the tumor region in living mice was irradiated by 808 nm laser with the power intensity of 0.3

W/cm^2 (the maximum exposure limit of skin to laser irradiation at 808 nm) for 5 min. Upon laser irradiation, the temperature of tumor region for $DSPN_5$ or PEG-PCB treated mice gradually increased (Fig. 5a, b), which was significantly higher than that for saline treated group at all time points. The temperature of tumor for PEG-PCB or $DSPN_5$ treated mice reached a plateau after laser irradiation for 2 min, and the mean temperature of tumor for SPN (59.6 ℃) or $DSPN_5$ treated mice (60.5 ℃) was about 1.5-fold of that for saline treated mice (39.3 ℃). Despite the higher in vitro photothermal maximum temperature of $DSPN_5$ relative to PEG-PCB (Fig. 2d), no significant difference of tumor temperature was observed between PEG-PCB and $DSPN_5$ treated mice, which might be attributed to the reduced accumulation of $DSPN_5$ in tumor region as indicated by the lower TLR of $DSPN_5$ than PEG-PCB (Fig. S6, supporting information).

To evaluate and compare the antitumor effect of PEG-PCB and $DSPN_5$, the volumes of tumors in living mice were continuously measured for 16 days (Fig. 5c). Without laser irradiation, tumors in $DSPN_5$ treated mice grew much slower than those for saline or PEG-PCB treated mice, indicating the certain level of antitumor effect of $DSPN_5$ by chemotherapy. With laser irradiation, PEG-PCB inhibited the growth of tumors for the first 6 days while failed at later time points, suggesting the limited antitumor effect of PEG-PCB mediated PTT. In comparison, only $DSPN_5$ mediated PTT completely inhibited the growth of tumors throughout the experimental period. The superior antitumor capability of $DSPN_5$ over PEG-PCB should be attributed to the synergistic effect resulted from the combination of chemotherapy and PTT. No significant weight loss was observed for all groups (Fig. 5d), indicating the safety of all treatments to mice.

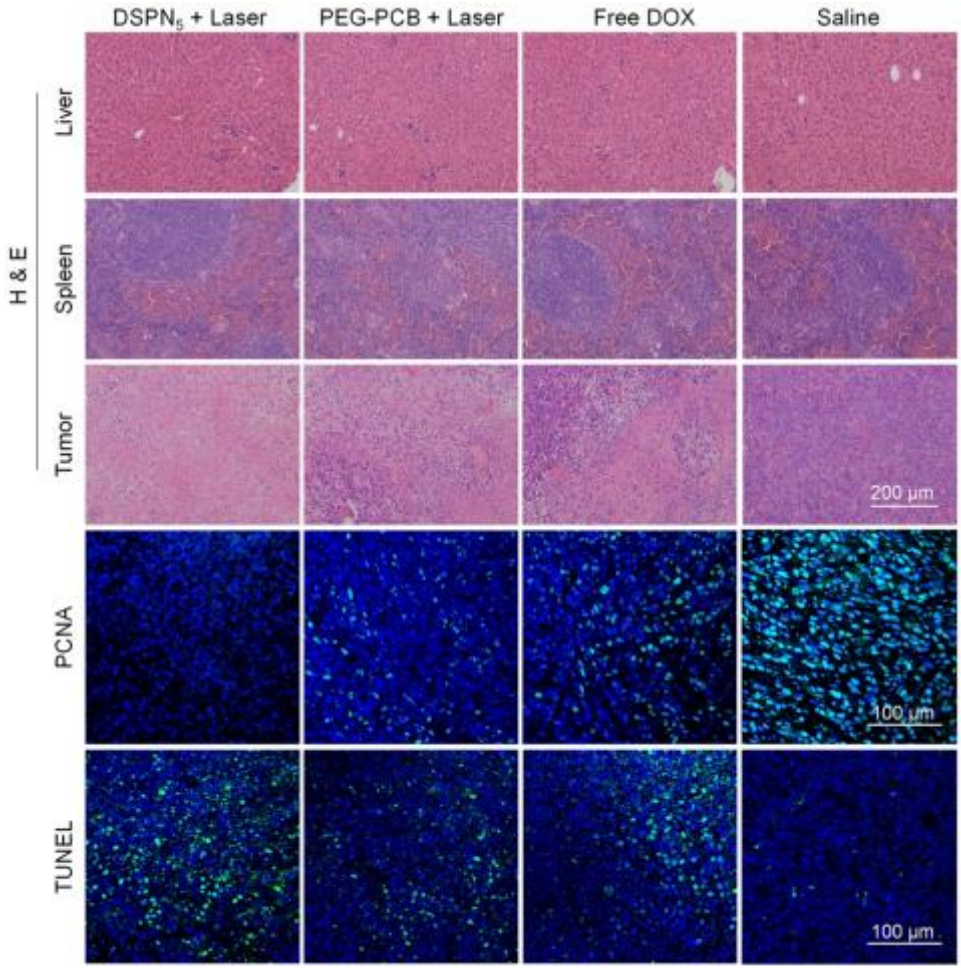

Fig. 6. Histological analysis. (a) H & E staining of livers, spleens and tumors for 4T1 tumor-bearing mice at day 16 after photothermal treatment with saline, free DOX, PEG-PCB, or $DSPN_5$. (b) Fluorescence PCNA and (c) TUNEL staining of tumors on 4T1 tumor-bearing mice at 16 d after photothermal treatment with saline, free DOX, PEG-PCB, or $DSPN_5$. Green fluorescence indicated signals of PCNA and TUNEL staining while blue fluorescence indicated nucleus staining.

To further validate the enhanced therapeutic effect of $DSPN_5$, all the mice were sacrificed at day 16 and histological analysis was performed on tumors and different organs by hematoxylin and eosin (H & E) staining, fluorescent proliferating cell nuclear antigen (PCNA) and TdT-mediated dUTP-biotin nick end labeling (TUNEL) staining. No noticeable histopathological damage was found in the liver or spleen of mice treated with free DOX, PEG-PCB, and $DSPN_5$

after PTT, while typical nuclear dissociation was clearly observed in tumor tissues of the same groups, with the overall severest dissociation found in $DSPN_5$ injected mice after PTT treatment (Fig. 6a). Besides, PCNA staining of tumor regions on mice demonstrated that the reproduction capacity of cancer cells was reduced in free DOX, PEG-PCB, or $DSPN_5$ treated mice after PTT (Fig. 6b), which was not observed saline treated mice without laser irradiation. In comparison with the sparse green fluorescent dots observed in free DOX or PEG-PCB treated mice, no fluorescent dots could be found in $DSPN_5$ treated group, which implied the minimum proliferation capability of cancer cells caused by chemo-photothermal therapy. Similarly, TUNEL staining of tumor region of mice showed the evident apoptosis of cancer cells observed in free DOX, PEG-PCB, or $DSPN_5$ treated mice after PTT (Fig. 6c). As indicated by the stronger green fluorescence in the tumor tissue, $DSPN_5$ caused severer apoptosis than PEG-PCB and free DOX. The outcome of histological analysis validated at cellular level the superiority of $DSPN_5$ over PEG-PCB and free DOX for antitumor effect, which was consistent with the result of *in vivo* antitumor experiments (Fig. 5c).

3. Conclusion

We have demonstrated a simplified theranostic nanoagent $DSPN_5$ for NIR fluorescence/PA imaging guided chemo-photothermal therapy. Such a concise design was based on an amphiphilic polymer PEG-PCB synthesized by PEGylation of semiconducting polymer via click chemistry. By virtue of the hydrophobic π-conjugated backbone, PEG-PCB not only acted as the contrast agent for both NIR fluorescence and PA imaging, but also served as the therapeutic agent for PTT as well as the drug delivery system for chemotherapy. Taking advantage of such trifunctionality, PEG-PCB was utilized to encapsulate DOX to obtain the greatly simplified nanotheranostic system ($DSPN_5$) with only dual components but multimodal theranostic capabilities. Due to the small size of nanoparticle, $DSPN_5$ was able to passively accumulate in the tumor site of living mice via EPR effect, allowing for effective NIR

fluorescence and PA imaging of tumor. After systemic administration of $DSPN_5$, the PA amplitude of tumor region on $DSPN_5$-treated mice could be 3.8-fold higher than that of the tumor background before systemic administration. Moreover, both *in vitro* and *in vivo* characterization of combination therapy revealed the superior antitumor efficacy of $DSPN_5$ over PEG-PCB or free DOX owning to the synergistic effect of chemotherapy and PTT. Superior to PEG-PCB mediated PTT or $DSPN_5$ mediated chemotherapy, $DSPN_5$ mediated chemo-photothermal therapy totally inhibited the tumor growth during experimental period, which was further validated at cellular level by histological analysis.

Our study thus provides a molecular engineering approach to integrate desired properties into one polymer for multimodal nanotheranostics. Because the side chains of amphiphilic SPs can be easily modified with Fluorine-19, further integration of magnetic resonance imaging (MRI) into the system could be feasible. In addition to chemotherapy drugs, other therapeutic agents such as immunoadjuvants can also be encapsulated into such polymer for other therapeutic purpose.

4. Experimental Section

Chemicals: All chemicals were purchased from Sigma-Aldrich unless otherwise mentioned.

Synthesis of PCB-Br: 2,6-dibromo-4,4-bis(6-bromohexyl)-4H-cyclopenta[2,1-b:3,4-b']dithiophene (50 mg, 0.075 mmol), 4,7-bis(4,4,5,5-tetramethyl-1,3,2-dioxaborolan-2-yl)benzo[c][1,2,5]thiadiazole (28 mg, 0.075 mmol), $Pd(PPh_3)_4$ (5.5 mg, 0.052 mmol) and K_2CO_3 (122.49 mg, 0.75 mmol) were placed in a 50 mL Schlenk tube. Then toluene (2.5 mL) with methyltrioctylammonium chloride (1 mg) and water (1.25 mL) were added to the Schlenk tube subsequently. The mixture was degassed by freeze-pump-thaw circles for three times. The reaction was carried out at 100 ºC under nitrogen atmosphere for 2 h. Then the solvent was removed under reduce pressure. The obtained solid was re-dissolved by excess dichloromethane and washed with water for three times. The organic phase was concentrated

and precipitated into excess methanol. The obtained solid was washed three times by methanol and then dried under vacuum to obtain product. ^{1}H NMR (300 MHz, $CDCl_3$) δ 8.12 (s, 1H), 7.89 (s, 1H), 7.61 (s, 2H), 3.33 (s, 3H), 1.90 (d, *J* = 93.0 Hz, 8H), 1.25 (s, 12H), 0.87 (d, *J* = 7.7 Hz, 4H).

Synthesis of PCB-N_3: SP-Br (10 mg) and sodium azide (4 mg) were dissolved in a mixture of THF (12 mL) and DMF (6 mL). The mixture was stirred at 25 ºC overnight. After that the solvent was removed under reduced pressure, an excess of dichloromethane was added to the residue. The resulted solution was washed three times with water and the organic phase was collected to dry over Na_2SO_4. The dichloromethane was removed and SP-N_3 was obtained. 1H NMR (300 MHz, CDCl3) δ 8.11 (s, 1H), 7.89 (d, J = 8.5 Hz, 1H), 7.72 – 7.41 (m, 2H), 3.18 (s, 3H), 2.02 (s, 4H), 1.28 (d, J = 17.3 Hz, 18H), 0.87 (d, J = 6.9 Hz, 3H).

Synthesis of PEG-PCB: SP-N_3 (10 mg) was dissolved in THF (12 mL). CuBr (11 mg), PMDETA (66.8 mg) and methoxy-PEG-alkyne (M_n = 2000, 150 mg) were added into previous solution subsequently. The reaction was carried out at room temperature under nitrogen atmosphere for 48 h. After that the solvents were removed under reduced pressure and the remaining residue was dissolved into water. The resulted solution was dialysis against DI water to remove the salt and excess methoxy-PEG-alkyne in the system. The SP-PEG was obtained after lyophilization. ^{1}H NMR (300 MHz, $CDCl_3$) δ 7.71 (s, 1H), 7.61 (s, 1H), 7.53 – 7.42 (m, 2H), 4.00 – 3.39 (m, 320H), 1.76 (d, *J* = 53.7 Hz, 32H), 1.31 (d, *J* = 33.2 Hz, 32H), 0.87 (d, *J* = 7.3 Hz, 24H).

Preparation of PEG-PCB Nanoparticles: PEG-PCB (1 mg) was dissolved in 1 mL THF by bath sonication. The obtained solution (1 mg/mL) was rapidly injected into a mixture of deionized water (9 mL) and THF (1 mL) solution under continuous sonication at a power output of 110 W for 1 min. THF in the solution was then removed by a nitrogen flow. The obtained solution was filtrated through a 0.22 μm PCDF syringe driven filter (Millipore). The PEG-PCB

solution was then concentrated by centrifugation at 2600 rpm for 25 min and subsequently diluted to different concentrations by 1 × PBS (pH = 7.4) for further use.

Preparation of DSPN$_5$: DSPN$_5$ was prepared via nanoprecipitation of DOX and PEG-PCB under controlled pH condition. DOX hydrochloride (DOX·HCl, 2 mg) was first dissolved in dimethyl sulfoxide (DMSO) (0.2 mL). Triethylamine (5 μL) was then added to the DOX·HCl DMSO solution (10 mg/mL) under bath sonication for 10 min. The resulted solution was subsequently mixed with the PEG-PCB solution in THF (1 mL, 1mg/mL). The obtained mixture was dialyzed in 1 × PBS buffer (pH = 7.4) for 48 h to remove excess free DOX. The resulted DSPN$_5$ solution was purified by filtration through a 0.22 μm PCDF syringe driven filter (Millipore) and then concentrated by ultrafiltration. Concentration of DOX encapsulated into nanoparticles was quantified by the absorbance of DSPN$_5$ at 500 nm after subtracting the absorbance of PEG-PCB at this wavelength. DSPN$_5$ was lyophilized followed by reconstitution to evaluate the LC. LC was calculated by the following equation: weight of encapsulated DOX / weight of DSPN$_5$ × 100%. Weight of encapsulated DOX was measured by UV-vis spectrometer.

Characterization of Nanoparticles: ^{1}H NMR spectra were obtained by Bruker Avance II 300 MHz NMR with $CDCl_3$ as the solvent. DLS was conducted on a Malvern Nano-ZS Particle Sizer. TEM images were acquired by a JEM 1400 transmission electron microscope with the accelerating voltage ranging from 40 to 120 kV. UV-Vis absorption spectra were recorded by Shimadzu UV-2450 spectrometer. Fluorescence spectra were obtained by Fluorolog 3-TCSPC spectrofluorometer (Horiba Jobin Yvon). An 808 nm high power NIR laser (operating mode, CW; output power after fiber, 2.5 W; LED display; diode current, multimode fiber; fiber core diameter, 400 μm; fiber connector, SMA905, with tunable laser driver module of 0-100%) purchased from CNI Co., Ltd. was used for PTT treatments. The laser power output was

measured by power meter. IR thermal images was captured by photothermal camera FLIR T420.

PA Instrumentation: An optical parametric oscillator (OPO) (Continuum, Surelite) pumped by a Q-switched 532 nm Nd: YAG laser was used as the laser source to generate tunable laser pulses within 680-900 nm wavelength range with 100 mJ/pulse energy at 10 Hz repetition rate. Nanoparticle solution was placed inside a low-density polyethylene (LDPE) tube with an inner diameter (i.d.) of 0.59 mm and an outer diameter (o.d.) of 0.78 mm. The LDPE tube containing samples and the ultrasound transducer (UST) (V323-SU/2.25MHz, 13 mm active area, and 70% nominal bandwidth, Panametrics) were both immersed in water to couple PA signals to UST. The LDPE tube was irradiated with laser pulses of wavelengths ranging from 680 to 920 nm with 10 nm increment. PA signals were collected by UST, amplified with a gain of 50 dB, and then band pass filtered (1-10 MHz) by a pulse/receiver unit (Olympus-NDT, 5072PR).

In Vitro PTT of Nanoparticles: 200 μL of PEG-PCB (PCB, 10 μg/mL), $DSPN_5$ (PCB, 10 μg/mL; DOX, 50 μg/mL), free DOX (DOX, 50 μg/mL), and PBS solutions were exposed to 808 nm laser with the power intensity of 1 W/cm^2, respectively. Temperature of solution was recorded every 20 s by an IR thermal camera until it reached the maximum (6 min).

In Vitro Drug Release Property of $DSPN_5$: 1 mL $DSPN_5$ solution (PCB, 0.2 mg/mL; DOX, 1 mg/mL) was filled into dialysis tubing (MW, 3000) which was then sealed and immersed in 5 mL PBS buffer of different pH conditions (pH = 5.5, 6.5, and 7.4), respectively. The dialysis reservoir was incubated in 37 ℃ water bath with constant shaking. At designated time points, the PBS buffer was removed to quantify the amount of released DOX while another 5 mL fresh PBS buffer was added to the dialysis reservoir for further study. The concentration of released DOX was measured by UV-Vis absorption spectroscopy.

Cell Culture and Cell Imaging: 4T1 mammary carcinoma cells were purchased from the American Type Culture Collection (ATCC). 4T1 cells were cultured in Dulbecco's Modified Eagle Medium (DMEM) with 10% fetal bovine serum (FBS) and antibiotics (10 U/mL penicillin and 10 mg/mL streptomycin) in an atmosphere of 5% CO_2 and 95% humidified air at 37 ℃. The cells were seeded in confocal dishes and incubated with PBS, PEG-PCB (PCB, 10 μg/ml), and $DSPN_5$ (PCB, 10 μg/ml; DOX, 50 μg/ml) respectively for 12 h before replacement of medium with fresh DMEM and nuclei staining by DAPI. Confocal images were captured by a LSM710 confocal laser scanning microscope (Carl Zeiss, Germany) with the excitation wavelength of 405 nm for DAPI, 488 nm for DOX and 633 nm for PCB.

In Vitro Chemo-Photothermal Therapy: Cells were seeded in 96-well plates (6000 cells in 200 μL DMEM per well) for 24 h, and then free DOX, PEG-PCB, or $DSPN_5$ (final PCB concentration 2, 5, 7, 10, and 15 μg/mL; final DOX concentration 10, 25, 35, 50, and 75 μg/mL) was added to the culture medium of cells separately. After incubation for 12 h, cells were treated with or without laser irradiation of 1 W/cm^2 for 6 min. After PTT treatment, cells were incubated for another 12 h. Then the medium was removed and fresh DMEM with MTS (0.1 mg/mL, 20 μL/well) was added to cells. After incubation for 4 h, the absorbance of MTS at 490 nm was measured by a SpectraMax M5 microplate/cuvette reader and the cell viability was quantified by the ratio of the absorbance of cells incubated with samples to that of control cells incubated with DMEM only.

Tumor Mouse Model: All animal experiments were performed in compliance with the guidelines established by Tianjin Committee of Use and Care of Laboratory Animals and the overall project protocols were approved by the Animal Ethics Committee of Nankai University. To establish tumors in six-week-old BALB/c mice, two million 4T1 cells suspended in 50 mL of 50 v/v% mixture of Matrigel in supplemented DMEM (10% FBS, 1% pen/strep, 100 U/mL penicillin, and 100 μg/mL streptomycin) were injected subcutaneously in the shoulders of the

mouse. Tumors were grown until a single aspect was ≈ 7 mm (10-15 days) before used for *in vivo* imaging and chemo-photothermal treatments.

In Vivo Fluorescence Imaging: Whole-body fluorescence imaging of mice was conducted by a Cri Maestro whole animal imaging system (Caliper Life Sciences, Hopkinton, MA). BALB/c mice bearing xenograft 4T1 tumors were administered with PEG-PCB (PCB, 30 μg per mouse) (n = 3) or $DSPN_5$ (PCB, 30 μg; DOX, 150 μg per mouse) (n = 3) through tail vein injection. Fluorescence images of mice were acquired at different time points (2, 4, 6, 8, 24 h) post-injection of nanoparticles. Quantification of fluorescence in each image was performed by Nuance software.

In Vivo PA Imaging: PA imaging of tumor region were performed by the Endra Nexus128 PA imaging system to acquire images at 680 nm. 4T1 tumor xenografted BALB/c mice were first anesthetized by 2% isoflurane in oxygen and then placed in the imaging system to determine the endogenous PA signal of tumor region before administration of samples. PEG-PCB (PCB, 30 μg per mouse) (n = 3), $DSPN_5$ (PCB, 30 μg; DOX, 150 μg per mouse) (n = 3), or saline (150 μL) (n = 3) were then systematically administered through tail vein injection. Data were acquired through a continuous model that tool 12 s to obtain one data set. 3D PA images were reconstructed offline using data acquired from all 128 transducers at each view and back-projection algorithm. The algorithm corrects for pulse-to-pulse variations in the laser intensity and small changes in the temperature that affect acoustic velocity in the water.

In Vivo Chemo-Photothermal Therapy: 4T1 tumor xenografted BALB/c mice were systemically administered with PEG-PCB (PCB, 30 μg per mouse) (n = 3), $DSPN_5$ (PCB, 30 μg; DOX, 150 μg per mouse) (n = 3), free DOX (DOX, 150 μg per mouse) (n = 3), or saline (n = 3) via a single tail vein injection. At 6 h post injection, tumor regions of living mice were exposed or without exposure to 808 nm laser of 0.3 W/cm^2. IR thermal camera was used to

record the temperature change of the tumor every 15s for 5 min after irradiation. The tumor size was measured by caliper every other day and calculated as follows: volume = (tumor length) × (tumor width)^2/2. Relative tumor size was calculated as V/V_0 (V_0 was the initial tumor volume). Mice with tumors larger than 1000 mm^3 should be euthanized according to the standard animal protocol.

Biodistribution Method: After 24 h post-injection of PEG-PCB (PCB, 30 μg per mouse) (n = 3) or $DSPN_5$ (PCB, 30 μg; DOX, 150 μg per mouse) (n = 3), the mice were sacrificed by CO_2 asphyxiation and tumor, heart, liver, spleen, lung, kidney, skin, muscle, and bones were harvested for *ex vivo* fluorescence imaging to quantify the biodistribution of nanoparticles.

Histological Studies: After 16 days of PTT, the mice treated with PEG-PCB (PCB, 30 μg per mouse) (n = 3), $DSPN_5$ (PCB, 30 μg; DOX, 150 μg per mouse) (n = 3), or saline (n = 3) were sacrificed. The tumor, liver, and spleen were fixed in 4% formalin. Paraffin embedded sectioning was then performed for H&E staining. The obtained slices were next exa mined under a digital microscope (Leica QWin). As for PCNA staining, sliced formalin-fixed tumor samples were used for confocal immunofluorescent analysis by PC10 Mouse mAb (#2586, Cell Signaling Technology). Fixed tumor sections were treated following the protocol of In Situ Cell Death Detection Kit (Roche Applied Science) for TUNEL apoptosis staining and Hoechst 33342 was used for nuclear counterstaining.

Data Analysis: *In vivo* PA signal intensities were measured by region-of-interest (ROI) anal ysis using OsiriX. Fluorescence signal intensities were measured by ROI analysis using ImageJ. Results were expressed as the mean ± SD deviation unless otherwise stated. All statistical calculations were performed using GraphPad Prism v.5 (GraphPad Software, Inc., CA, USA).

Acknowledgements

K.P. thanks Nanyang Technological University (Start-Up grant: NTU-SUG: M4081627.120) and Singapore Ministry of Education (Academic Research Fund Tier 1: RG133/15 M4011559 and Academic Research Fund Tier 2 MOE2016-T2-1-098) for the financial support. M.P. thanks the Singapore Ministry of Health's National Medical Research Council (NMRC/OFIRG/0005/2016: M4062012) for the financial support. D.D. thanks the National Basic Research Program of China (2015CB856503) and the NSFC (51622305) for the financial support.

Appendix A. Supplementary data

Supplementary data related to this article can be found at Biomaterials.

References

[1] H. Chen, W. Zhang, G. Zhu, J. Xie, X. Chen, Rethinking cancer nanotheranostics, Nat. Rev. Mater. 2 (2017) 17024.

[2] Z. Cheng, A. Al Zaki, J.Z. Hui, V.R. Muzykantov, A. Tsourkas, Multifunctional nanoparticles: cost versus benefit of adding targeting and imaging capabilities, Science 338 (2012) 903-910.

[3] X. Zhao, C.-X. Yang, L.-G. Chen, X.-P. Yan, Dual-stimuli responsive and reversibly activatable theranostic nanoprobe for precision tumor-targeting and fluorescence-guided photothermal therapy, Nat. Commun. 8 (2017) 14998.

[4] C. Li, A targeted approach to cancer imaging and therapy, Nat. Mater. 13 (2014) 110-115.

[5] H. Liu, K. Wang, C. Yang, S. Huang, M. Wang, Multifunctional polymeric micelles loaded with doxorubicin and poly(dithienyl-diketopyrrolopyrrole) for near-infrared light-controlled chemo-phototherapy of cancer cells, Colloids Surf., B 157 (2017) 398-406.

[6] D. Luo, K.A. Carter, A. Razi, J. Geng, S. Shao, D. Giraldo, et al., Doxorubicin encapsulated in stealth liposomes conferred with light-triggered drug release, Biomaterials 75 (2016) 193-202.

[7] D. Miranda, K. Carter, D. Luo, S. Shao, J. Geng, C. Li, et al., Multifunctional Liposomes for Image-Guided Intratumoral Chemo-Phototherapy, Adv. Healthcare Mater. (2017) 1700253.

[8] H. Liu, D. Chen, L. Li, T. Liu, L. Tan, X. Wu, et al., Multifunctional gold nanoshells on silica nanorattles: a platform for the combination of photothermal therapy and chemotherapy with low systemic toxicity, Angew. Chem. Int. Edit. 50 (2011) 891-895.

[9] H. Wang, P. Agarwal, S. Zhao, J. Yu, X. Lu, X. He, A biomimetic hybrid nanoplatform for encapsulation and precisely controlled delivery of theranostic agents, Nat. Commun. 6 (2015) 10081.

[10] H. Yu, Z. Cui, P. Yu, C. Guo, B. Feng, T. Jiang, et al., pH-and NIR light-responsive micelles with hyperthermia-triggered tumor penetration and cytoplasm drug release to reverse doxorubicin resistance in breast cancer, Adv. Funct. Mater. 25 (2015) 2489-2500.

[11] J. Conde, N. Oliva, Y. Zhang, N. Artzi, Local triple-combination therapy results in tumour regression and prevents recurrence in a colon cancer model, Nat. Mater. 15 (2016) 1128-1138.

[12] V. Ntziachristos, J. Ripoll, L.V. Wang, R. Weissleder, Looking and listening to light: the evolution of whole-body photonic imaging, Nat. Biotechnol. 23 (2005) 313-320.

[13] A.L. Antaris, H. Chen, K. Cheng, Y. Sun, G. Hong, C. Qu, et al., A small-molecule dye for NIR-II imaging, Nat. Mater. 15 (2016) 235-242.

[14] G. Hong, A.L. Antaris, H. Dai, Near-infrared fluorophores for biomedical imaging, Nat. Biomed. Eng. 1 (2017) 0010.

[15] A.M. Smith, M.C. Mancini, S. Nie, Second window for in vivo imaging, Nat. Nanotechnol. 4 (2009) 710-711.

[16] V. Ntziachristos, D. Razansky, Molecular imaging by means of multispectral optoacoustic tomography (MSOT), Chem. Rev. 110 (2010) 2783-2794.

[17] L.V. Wang, J. Yao, A practical guide to photoacoustic tomography in the life sciences, Nat. Methods 13 (2016) 627-638.

[18] J. Weber, P.C. Beard, S.E. Bohndiek, Contrast agents for molecular photoacoustic imaging, Nat. Methods 13 (2016) 639-650.

[19] P.K. Upputuri, M. Pramanik, Recent advances toward preclinical and clinical translation of photoacoustic tomography: a review, J. Biomed. Opt. 22 (2017) 041006.

[20] J. Wang, F. Chen, S.J. Arconada-Alvarez, J. Hartanto, L.-P. Yap, R. Park, et al., A nanoscale tool for photoacoustic-based measurements of clotting time and therapeutic drug monitoring of heparin, Nano Lett. 16 (2016) 6265-6271.

[21] S.E. Bohndiek, L.S. Sasportas, S. Machtaler, J.V. Jokerst, S. Hori, S.S. Gambhir, Photoacoustic tomography detects early vessel regression and normalization during ovarian tumor response to the antiangiogenic therapy trebananib, J. Nucl. Med. 56 (2015) 1942-1947.

[22] X.-R. Song, X. Wang, S.-X. Yu, J. Cao, S.-H. Li, J. Li, et al., Co9Se8 nanoplates as a new theranostic platform for photoacoustic/magnetic resonance dual-modal-imaging-guided chemo-photothermal combination therapy, Adv. Mater. 27 (2015) 3285-3291.

[23] T. Liu, C. Wang, X. Gu, H. Gong, L. Cheng, X. Shi, et al., Drug delivery with PEGylated MoS2 nano-sheets for combined photothermal and chemotherapy of cancer, Adv. Mater. 26 (2014) 3433-3440.

[24] Y. Wang, K. Wang, J. Zhao, X. Liu, J. Bu, X. Yan, et al., Multifunctional mesoporous silica-coated graphene nanosheet used for chemo-photothermal synergistic targeted therapy of glioma, J. Am. Chem. Soc. 135 (2013) 4799-4804.

[25] M. Zhou, S. Liu, Y. Jiang, H. Ma, M. Shi, Q. Wang, et al., Doxorubicin-loaded single wall nanotube thermo-sensitive hydrogel for gastric cancer chemo-photothermal therapy, Adv. Funct. Mater. 25 (2015) 4730-4739.

[26] L. Zhang, Y. Chen, Z. Li, L. Li, P. Saint-Cricq, C. Li, et al., Tailored synthesis of octopus-type Janus nanoparticles for synergistic actively-targeted and chemo-photothermal therapy, Angew. Chem. Int. Edit. 55 (2016) 2118-2121.

[27] T. Zheng, G.G. Li, F. Zhou, R. Wu, J.-J. Zhu, H. Wang, Gold-nanosponge-based multistimuli-responsive drug vehicles for targeted chemo-photothermal therapy, Adv. Mater. 28 (2016) 8218-8226.

[28] J. Song, X. Yang, O. Jacobson, L. Lin, P. Huang, G. Niu, et al., Sequential drug release and enhanced photothermal and photoacoustic effect of hybrid reduced graphene oxide-loaded ultrasmall gold nanorod vesicles for cancer therapy, ACS Nano 9 (2015) 9199-9209.

[29] M. Zheng, C. Yue, Y. Ma, P. Gong, P. Zhao, C. Zheng, et al., Single-step assembly of DOX/ICG loaded lipid–polymer nanoparticles for highly effective chemo-photothermal combination therapy, ACS Nano 7 (2013) 2056-2067.

[30] X. Meng, Z. Liu, Y. Cao, W. Dai, K. Zhang, H. Dong, et al., Fabricating aptamer-conjugated PEGylated-MoS2/Cu1.8S theranostic nanoplatform for multiplexed imaging diagnosis and chemo-photothermal therapy of cancer, Adv. Funct. Mater. 27 (2017) 1605592.

[31] K. Pu, J. Mei, J.V. Jokerst, G. Hong, A.L. Antaris, N. Chattopadhyay, et al., Diketopyrrolopyrrole-based semiconducting polymer nanoparticles for in vivo photoacoustic imaging, Adv. Mater. 27 (2015) 5184-5190.

[32] K. Pu, A.J. Shuhendler, J.V. Jokerst, J. Mei, S.S. Gambhir, Z. Bao, et al., Semiconducting polymer nanoparticles as photoacoustic molecular imaging probes in living mice, Nat. Nanotechnol. 9 (2014) 233-239.

[33] A.J. Shuhendler, K. Pu, L. Cui, J.P. Uetrecht, J. Rao, Real-time imaging of oxidative and nitrosative stress in the liver of live animals for drug-toxicity testing, Nat. Biotechnol. 32 (2014) 373-380.

[34] L. Feng, C. Zhu, H. Yuan, L. Liu, F. Lv, S. Wang, Conjugated polymer nanoparticles: preparation, properties, functionalization and biological applications, Chem. Soc. Rev. 42 (2013) 6620-6633.

[35] K. Sun, Y. Tang, Q. Li, S. Yin, W. Qin, J. Yu, et al., In vivo dynamic monitoring of small molecules with implantable polymer-dot transducer, ACS Nano 10 (2016) 6769-6781.

[36] C.-S. Ke, C.-C. Fang, J.-Y. Yan, P.-J. Tseng, J.R. Pyle, C.-P. Chen, et al., Molecular engineering and design of semiconducting polymer dots with narrow-band, near-infrared emission for in vivo biological imaging, ACS Nano 11 (2017) 3166-3177.

[37] J. Yu, Y. Rong, C.-T. Kuo, X.-H. Zhou, D.T. Chiu, Recent advances in the development of highly luminescent semiconducting polymer dots and nanoparticles for biological imaging and medicine, Anal. Chem. 89 (2017) 42-56.

[38] Y. Jiang, K. Pu, Advanced photoacoustic imaging applications of near-infrared absorbing organic nanoparticles, Small (2017) 1700710.

[39] Y. Lyu, Y. Fang, Q. Miao, X. Zhen, D. Ding, K. Pu, Intraparticle molecular orbital engineering of semiconducting polymer nanoparticles as amplified theranostics for in vivo photoacoustic imaging and photothermal therapy, ACS Nano 10 (2016) 4472-4481.

[40] Y. Lyu, C. Xie, S.A. Chechetka, E. Miyako, K. Pu, Semiconducting polymer nanobioconjugates for targeted photothermal activation of neurons, J. Am. Chem. Soc. 138 (2016) 9049-9052.

[41] Y. Lyu, X. Zhen, Y. Miao, K. Pu, Reactivity-based semiconducting polymer nanoprobes for photoacoustic imaging of protein sulfenic acids, ACS Nano 11 (2016) 358-367.

[42] Q. Miao, Y. Lyu, D. Ding, K. Pu, Semiconducting oligomer nanoparticles as an activatable photoacoustic probe with amplified brightness for in vivo imaging of pH, Adv. Mater. 28 (2016) 3662-3668.

[43] C. Xie, X. Zhen, Q. Lei, R. Ni, K. Pu, Self-assembly of semiconducting polymer amphiphiles for in vivo photoacoustic imaging, Adv. Funct. Mater. 27 (2017) 1605397.

[44] C. Yin, X. Zhen, Q. Fan, W. Huang, K. Pu, Degradable semiconducting oligomer amphiphile for ratiometric photoacoustic imaging of hypochlorite, ACS Nano 11 (2017) 4174-4182.

[45] C. Yin, H. Zhu, C. Xie, L. Zhang, P. Chen, Q. Fan, et al., Organic nanoprobe cocktails for multilocal and multicolor fluorescence imaging of reactive oxygen species, Adv. Funct. Mater. 27 (2017) 1700493.

[46] J. Zhang, X. Zhen, P.K. Upputuri, M. Pramanik, P. Chen, K. Pu, Activatable photoacoustic nanoprobes for in vivo ratiometric imaging of peroxynitrite, Adv. Mater. 27 (2016) 1604764.

[47] X. Zhen, C. Zhang, C. Xie, Q. Miao, K.L. Lim, K. Pu, Intraparticle energy level alignment of semiconducting polymer nanoparticles to amplify chemiluminescence for ultrasensitive in vivo imaging of reactive oxygen species, ACS Nano 10 (2016) 6400-6409.

[48] D.-D. Li, J.-X. Wang, Y. Ma, H.-S. Qian, D. Wang, L. Wang, et al., A donor–acceptor conjugated polymer with alternating isoindigo derivative and bithiophene units for near-infrared modulated cancer thermo-chemotherapy, ACS Appl. Mater. Inter. 8 (2016) 19312-19320.

[49] Y. Wang, Y. Xiao, R. Tang, Spindle-like polypyrrole hollow nanocapsules as multifunctional platforms for highly effective chemo–photothermal combination therapy of cancer cells in vivo, Chem. Eur. J 20 (2014) 11826-11834.

[50] D. Zhang, M. Wu, Y. Zeng, N. Liao, Z. Cai, G. Liu, et al., Lipid micelles packaged with semiconducting polymer dots as simultaneous MRI/photoacoustic imaging and photodynamic/photothermal dual-modal therapeutic agents for liver cancer, J. Mater. Chem. B 4 (2016) 589-599.

TOC

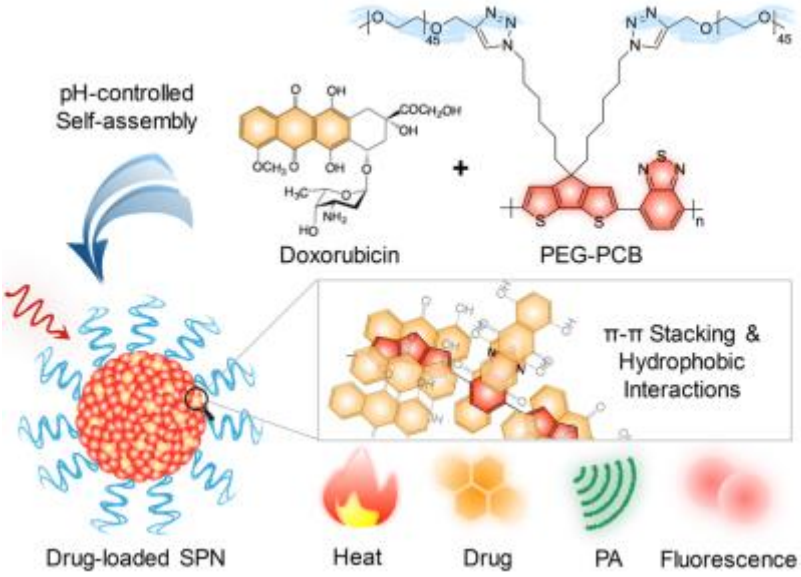
pH-controlled
Self-assembly
Doxorubicin
PEG-PCB
π-π Stacking &
Hydrophobic
Interactions
Drug-loaded SPN
Heat
Drug
PA
Fluorescence